Universal approach for diffusion quantification applied to lead halide perovskite single crystals

Jan Pospisil[1] · Lucie Marackova[1] · Oldrich Zmeskal[1] · Alexander Kovalenko[2]

Abstract

A universal approach to calculating diffusion coefficients in lead halide perovskite single crystals, which have ionic and mixed ionic–electronic conductivity, is proposed. Using impedance spectroscopy, it is demonstrated how to model a non-ideal Warburg element and transmission line equivalent circuit to identify ionic diffusion in the material. The proposed method is applicable to samples of any thickness and electrical properties. Additionally, it is shown how to overcome the challenges of low-frequency impedance measurement and the non-ideal behavior of the elements through extrapolative modeling and approximation.

1 Introduction

Understanding charge carrier dynamics in the material can be crucial for deep comprehension and handling of degradation and operational processes of electronic and optoelectronic devices. Lead halide perovskites, apart from being a semiconductor, additionally show pronounced ionic conductivity [1, 2], which is the result of ionic diffusion, and thus a non-uniform concentration of charged particles in the material. This type of charge transport appeared to be responsible for many unique properties of lead halide perovskite that had been long debated and various explanations had been suggested [3–6]. For instance, in [7, 8], it was proposed that capacitive anomalies at low and intermediate frequencies

can be associated with ionic migration in methylammonium lead bromide single crystals.

Widely reported and discussed [8], hysteresis in perovskite solar cells, despite many various suggestions in the past, [9] at the present moment is mainly associated with slow ionic charge transport [10, 11]. Several studies have reported [13–16] that halide perovskites containing IV-group B-cations have a discernible ionic contribution to the overall electrical transport characteristics.

Impedance spectroscopy investigation on lead halide perovskite films [17–19] revealed the presence of a low-frequency contribution, which was attributed to the migration of slow-moving charged species. Moreover, Warburg-like semi-infinite diffusion at low frequencies was observed in lead halide solar cell-like architecture under light illumination. This behavior is typical for mixed conductors [20], which is indirect evidence of moving species in the material. The ion migration hypothesis was supported by a large amount of evidence from detailed research. Ionic defect conductivity is well known in similar materials like metal oxide perovskites. Moreover, it was discovered that a cubic or orthorhombic shape correlates with high ionic conductivity [21, 22].

Following the aforesaid, charge carrier dynamics in single crystals is of utmost importance, as it corresponds to the intrinsic property of the material that helps to understand various processes and operational mechanisms [23, 24], such as operational and/or temporal stability [25, 26] of optical

✉ Alexander Kovalenko
  kovalale@fit.cvut.cz

  Jan Pospisil
  pospisilj@fch.vut.cz

  Lucie Marackova
  xcplesnikova@fch.vut.cz

  Oldrich Zmeskal
  zmeskal@fch.vut.cz

1   Faculty of Chemistry, Brno University of Technology, Purkyňova 118, Brno 61200, Czech Republic

2   Faculty of Information Technology, Czech Technical University in Prague, Thakurova 9, Prague 16000, Czech Republic

and electrical devices. In this regard, several great efforts have been done to explain charge carrier dynamics in perovskites [27, 28]; however, some of them were performed using complicated layered structures that can distort diffusion coefficient due to the interfacial influence, while others have limited applicability due to the complicated sample preparation. Moreover, in the case of the measurements provided on thin films, given an extremely long ionic diffusion range, the reduced dimensionality of samples dramatically affects the charge carrier dynamics in the material, requiring careful consideration in quantifying diffusion [29–31].

Here, we present a simple and universal approach for diffusion quantification applied to lead halide perovskite single crystals. Single crystals, prepared by inverse temperature crystallization [32], were used as they show exceptionally low intrinsic defect density [33] and generally are easy to synthesize. Nevertheless, we assume that the strategy described below allows direct monitoring and therefore quantifying of the ionic-related conductivity regardless of the presence of electronic current, and is applicable for an arbitrarily mixed conductor possessing ionic diffusion.

The material's resistive, capacitive, and inductive properties all contribute to its electrical response in the frequency–time domain. By understanding these response characteristics, we can explain various processes that are happening within the material. For this reason, impedance spectroscopy is a powerful tool that measures the electrical response, depending on the material's electrodynamic properties [34, 35]. By monitoring complex impedance values and phase shifts at various frequencies, this technique allows separating resistive, capacitive, and inductive current contributions by using appropriate mathematical modeling.

2 Methodology

2.1 Warburg-like diffusion model

While the dynamics of ionic processes are much slower than electronic ones, their characteristic features tend to appear at relatively low frequencies. Therefore, by locating characteristic turnover frequency, it is possible to quantify diffusion in the material. The model for diffusion quantification described by Peng et al. [28] fits well, for thin films when the sample thickness is less than the diffusion length. Lead halide perovskites are well known for their exceptionally long diffusion length in the range of micrometers [36]; thus, the above-mentioned model can be successfully applied for the films used for most optoelectronic devices, as their thickness rarely exceeds 0.5 um. However, for thicker films or single crystals, the model is not valid once the thickness of the sample is larger than the diffusion length. Moreover, this technique is barely applicable to measure diffusion

coefficients in materials with shorter diffusion lengths, e.g.. organic semiconductors [37].

In this paper, a sandwich structure was used, and the Warburg model of diffusion for flat parallel electrodes can be applied. A Warburg impedance element Z_W is nearly always associated with a charge-transfer resistance and a double-layer capacitance [38]. Therefore, once Warburg-like characteristics of the impedance response are observed, the diffusion coefficient can be determined. However, it can be difficult to identify a Warburg element in practice due to two main issues: non-ideality and the low-frequency range. In this regard, we denote non-ideal diffusion as 'Warburg-like diffusion'; later, we discuss why such diffusion is problematic to detect and evaluate.

2.1.1 Diffusion non-ideality

Mathematically, the Warburg element total impedance at equilibrium can be defined by the equation (1) [39], as the magnitude of the Warburg impedance is reversibly proportional to the square root of angular frequency according to:

$$Z_W = \sigma\omega^{-1/2} - j\sigma\omega^{-1/2}, \tag{1}$$

where Warburg coefficient σ is related to the concentrations and diffusion coefficients of the oxidized and reduced species (C_{ox}, C_{red}, D_{ox}, and D_{red}, respectively) by:

$$\sigma = \frac{RT}{n^2F^2A\sqrt{2}}\left(\frac{1}{C_{ox}D_{ox}^{1/2}} + \frac{1}{C_{red}D_{red}^{1/2}}\right), \tag{2}$$

where R is the gas constant (J/K/mol), T is the temperature (K), n is the number of exchanged electrons, F is the Faraday constant (C/mol), A is the area of the electrode (m^2/s), C_{ox} and C_{red} are the bulk concentrations of electroactive species in their oxidized, resp. reduced form (mol/m^3), and D_{ox}, and D_{red} are diffusion coefficients of oxidized, resp. reduced species (m^2/s).

Thus, the Warburg circuit element is typically associated with the existence of a linear relationship with a slope of –1/2 on the log of a Bode plot (log $|Z|$ versus log (ω)), and it exhibits a 45° phase shift. Moreover, in the case of ideal Warburg behavior, at the frequency range where the phase shift is frequency independent, plotting both real (R) and imaginary (X) part of the impedance Z versus $1/\omega^{1/2}$ results in two straight parallel lines where the slope is directly the Warburg coefficient σ. Warburg pseudocapacitance (C_W) cannot be regarded as a pure capacitor, because it is dependent on faradaic charge transfer across the interphase.

However, in the original study [39], Warburg reports smaller phase angles for the different electrodes used in the experiment; unfortunately, at the same time, the frequency range is not reported. A phase angle of 45° is a result of

deviation from a semi-infinite diffusion condition. Nevertheless, one can notice that experiments on real-life samples or devices (solar cells, batteries, detectors, etc.) often show non-ideal Warburg-like diffusion with phase angles, more often higher, or sometimes lower than –45°. Lower phase angles are associated with, for example, additional leakage currents that make the whole system less capacitive, while higher angles are a result of factors that add additional capacitive behavior, such as extra porosity, which can charge, like a capacitor, but will not be a part of the diffusion component.

In cases where diffusion is expected, such as lead halide perovskites as discussed in this paper, the diffusion model cannot be considered an ideal Warburg model. As a result, the dependencies of R and X on $1/\omega^{1/2}$ will not be linear or parallel, making it difficult to accurately estimate the diffusion coefficient.

As a result, the presence of diffusion may go undetected because the usual methods for identifying Warburg-like behavior will not be applicable. To detect diffusion in these cases, we propose the following approach:

- Find a low-frequency interval, where the phase shift is between 0° and –90° and frequency independent.
- Given the frequency interval meeting the previous condition, find a slope of $\ln(Z)$ vs $\ln(\omega)$, which gives a value of a so-called ideality factor k.
- Plot both R and X vs. $1/\omega^k$, which we denote as a *modified Warburg impedance plot*.

In this case, if the plots in the mentioned frequency range are linear, diffusion can be quantified. Note that R and X may not be parallel, which will be discussed later. However, it is worth noting that R and X may not be parallel, which will be discussed further on. As a result, the slopes for the real and imaginary parts of the impedance, σ_R and σ_X, respectively, are distinct.

Thus, total non-ideal Warburg-like impedance at the equilibrium can be defined by the equation (3):

$$Z_W = \sigma_R \omega^{-k} - j\sigma_X \omega^{-k}, \tag{3}$$

where σ_R and σ_X are non-ideal Warburg coefficients for resistance (R, Z_R) and reactance (X, Z_X), respectively. From equation 3, both real and imaginary parts of the impedance can be derived as follows:

$$\ln\left(Z_R\right) = \ln\left(\sigma_R\right) + k\ln(\omega), \tag{4}$$

$$\ln\left(Z_X\right) = \ln\left(\sigma_X\right) + k\ln(\omega). \tag{5}$$

Thus, by plotting $\ln\left(Z_R\right)$ or $\ln\left(Z_X\right)$ vs $\ln\left(\omega\right)$ (i.e., modified Bode plot for the real and imaginary parts of impedance as

a function of angular frequency), the ideality factor k can be easily determined from the slope of this dependence; moreover, from the intersection on the y-axis, the Warburg coefficient σ (representing the ideal case of the Warburg element) can be obtained at the same time.

2.1.2 Diffusion detection frequency

At a constant temperature, the diffusion coefficient mainly depends on the intrinsic characteristics of the material that define the diffusion coefficient [39]. The relation between the diffusion coefficient and the turnout frequency range on the impedance spectrum was previously discussed by Bisquert [40] and Janssen et. al [41]. Therefore, at the impedance spectrum, diffusion may occur in an extremely low-frequency range, micro-Hz or even nano-Hz. In an ideal case, the frequency interval where diffusion occurs should be in a range where the phase shift is negative and frequency independent, -45° as can be derived from equation 1. In non-ideal diffusion conditions, higher phase angles between 0° and -45° (more resistive behavior) may be caused by contact/interface non-idealities leading to charge carrier dispersion, while lower phase angles between -45° and -90° (more capacitive behavior) may occur in porous materials where pores act like capacitors that accumulate charges, but are not part of the diffusion component.

2.1.3 Warburg diffusion element equivalent circuit

As discussed above, using impedance spectroscopy for diffusion detection/quantification can be quite problematic, as the diffusion can appear at an extremely low-frequency range; therefore, measurements would last weeks and even longer, which is practically often not acceptable. However, the power of impedance spectroscopy lies in the ability to extrapolate using equivalent circuit modeling [35, 42]. Fortunately, equivalent circuit for both Warburg diffusion [43–46] and lead halide perovskites [18, 47–49] are well reported and described in the literature. Therefore, it is possible to get a hint on the equivalent circuit of the whole system. In the present paper, to fit impedance response within the frequency domain, an equivalent circuit, depicted in Fig. 1, was used.
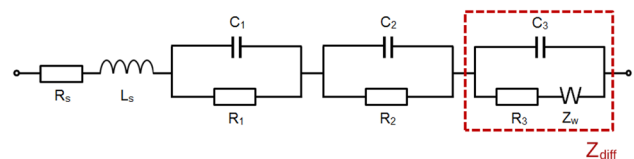

Fig. 1 Equivalent circuit for the Warburg diffusion element and perovskite single-crystal sandwich structure

The diffusion element was modeled according to the literature [50–53], and the complex impedance Z_{diff} of the electrical circuit including the Warburg diffusion element can be described by equation (6):

$$Z_{\text{diff}} = \frac{R_3 + \frac{(1-j)\sigma}{\omega^{0.5}}}{1 + j\omega C_3 \left[R_3 + \frac{(1-j)\sigma}{\omega^{0.5}} \right]}, \sigma = \frac{Z_0}{\sqrt{2}}, \quad (6)$$

where σ is the Warburg coefficient, Z_0 is the magnitude of the impedance at $\omega = 1$ rad/s, ω is the angular frequency, j is the imaginary unit, and R_3 and C_3 are the low-frequency resistance and capacitance, respectively, while the full impedance of the whole circuit can be defined as shown in equation (7):

$$Z = R_s + j\omega L_s + \frac{R_1}{1 + j\omega R_1 C_1} + \frac{R_2}{1 + j\omega R_2 C_2} + Z_{\text{diff}}, \quad (7)$$

where R_1 and C_1 are high-frequency resistance and capacitance, R_2 and C_2 are middle-frequency resistance and capacitance, Z_{diff} is the low-frequency complex impedance of the circuit consisting of the Warburg element, R_S is the series resistance, and L_S is the series inductance. Therefore, using the above-described relations for the full impedance Z, one can fit the impedance response in the frequency domain. Fitting precision for the current measurements is shown in supporting materials.

2.2 How do we quantify diffusion?

Given the above, we propose a protocol for Warburg-like diffusion quantification:

- Ideality factor k can be extracted correctly only if we know the behavior at very low frequencies, where the diffusion takes place (often nano Hz). To obtain k we need to fit the model to the existing data, using the equivalent circuit given in Fig. 1 defined by the correspondent equation6, resp. 7.
- Once we fit the model on the measured data, we are able to extrapolate the data down to nano Hz, to detect the potential diffusion frequency range where the phase angle is negative and frequency independent.
- From the slope of $\ln(Z)$ vs $\ln(f)$ or $\ln(\omega)$ at the frequency range obtained from above, the k coefficient can be obtained. It has to be noted that k can be obtained also from the phase angle, at the diffusion frequency range.
- The ideal case assumes linear regression on the $R - X$ plot vs. $\omega^{-1/2}$, where both resistance and reactance dependences are straight and parallel with respect to $\omega^{-1/2}$. However, in the case of non-ideal Warburg behavior, R and X are not parallel and non-linear, so the coefficient will depend on the frequency, and there will

be a significant difference between σ_R and σ_X resulting in the interpretation ambiguity once again.
- However, if we plot $R - X$ vs. ω^{--k}, it linearizes both dependencies and makes σ_R and σ_X almost equal.

After deriving σ_R and σ_X values, the diffusion can be easily quantified.

3 Results and discussion

In the ideal case, Warburg diffusion can be modeled using the so-called 'ideality factor' $k = 1/2$. Nevertheless, in 'real-world' samples having such a value for k is rather an exception. Usually, one can observe lower values because of any sort of leakage currents, and also higher values can be observed in the case of porous materials. In these cases, the Warburg coefficient σ is problematic to determine, as non-ideality results in a non-linear $R - X$ plot vs. $1/\omega^{0.5}$. We propose that in such cases, ideal factor 0.5 should be replaced by k factor; therefore, the plot should be represented as $R - X$ plot vs. $1/\omega^{0.5}$. As an example, let us analyze the data obtained from the $MAPbI_3$ perovskite monocrystal sandwich structure. In the first step, the diffusion frequency range has to be located. As we discussed above, in this range, the phase angle should be negative and frequency independent (Fig. 2b), the slope of $\ln(Z)$ vs $\ln(\omega)$ in this frequency range (Fig. 2a) gives us the ideality factor $k = 0.21$, i.e,. non-ideal Warburg behavior, and phase shift corresponds to approx. 21° at low frequencies.

After introducing $k = 0.21$, one can obtain both σ_R and σ_X modified Warburg constants. By the way, as described above, we can get the Warburg constant ω directly from the Bode plot according to equations (4) and (5). To quantify the Warburg coefficient, we finally used the mean value of σ_R and σ_X. As a demonstration, for $MAPbI_3$ perovskite single crystal with ideality factor equal to 0.21, the calculated Warburg coefficient (avg value) from the modified $R - X$ plot vs. $\omega^{--0.21}$ is approximately $\sigma_k = 2.29 \times 10^9/s^{0.21}$ ($\sigma_R = 3.43 \times 10^9/s^{0.21}$, $\sigma_X = 1.14 \times 10^9/s^{0.21}$). The determined Warburg coefficient (average value) from the modified Bode plot is approx. $\sigma = 2.49 \times 10^9/s^{0.5}$ ($\sigma_R = 3.73 \times 10^9/s^{0.5}$, $\sigma_X = 1.24 \times 10^9/s^{0.5}$).

To find a correlation between an ideal and a non-ideal Warburg behavior, we tested a large auto-generated set of models (for more details see Supporting Information) with the equivalent circuit described above in Fig. 1. A general trend between an ideal and a non-ideal Warburg component that follows a quadratic function, empirically defined by an equation $y = 1.647x^2 - -1.568x + 1.373$, is shown in Fig. 3a. Due to this relationship, the ideal Warburg element (and thus the final Warburg coefficient) can be easily estimated even if we have non-ideal Warburg behavior in our
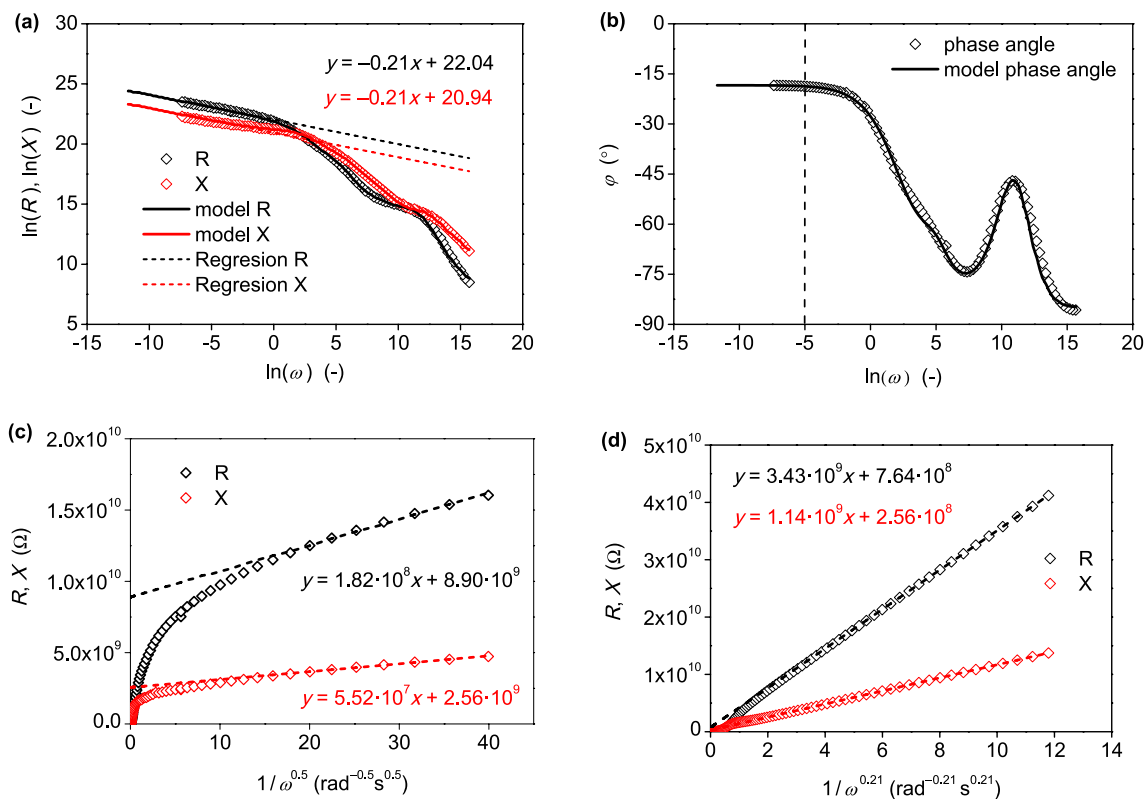
Fig. 2 A The modified Bode plot, points for real measured data, solid lines for modeled data up to 1 μHz, dashed lines for interpolation of data in low frequencies; **B** a phase shift between the real and imaginary part of Z plotted against $\ln(\omega)$ with a line indicating the area where the phase shift is independent of frequency; **C** a plot of the non-ideal Warburg-like impedance; **D** the modified plot of the non-ideal Warburg-like impedance using coefficient k for ideal or non-ideal behavior
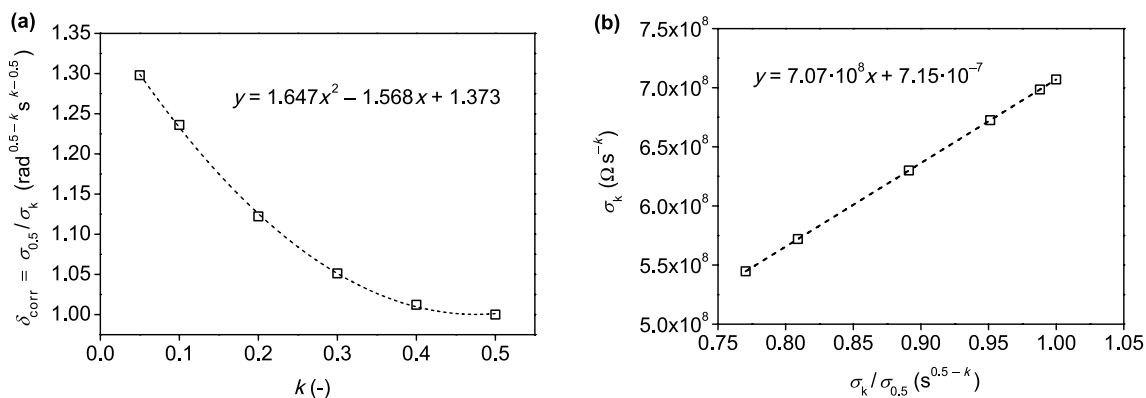
Fig. 3 A Correlation between an ideal and a non-ideal Warburg component. **B** The Warburg coefficients for a Warburg diffusion element equivalent circuit ($R_3 = 5G\Omega$, $C_3 = 1nF$, $Z_W = 1G\Omega$) with variable ideality factors and its slope which follows the standard value for an ideal Warburg component

system. However, what arises here is the Warburg coefficient unit, due to the different powers/roots for angular frequency in the graphs. In this regard, it is necessary to introduce a new correction factor $\delta_{corr} = \sigma_{0.5}/\sigma_k \left(rad^{0.5-k}\, s^{k-0.5}\right)$, which adjusts the finite unit of the Warburg coefficient (especially for purposes of non-ideal Warburg behavior) so that it is correct for evaluating the diffusion coefficient with its unit m^2/s.

As an example, according to these findings, the above-determined Warburg coefficient from the modified $R - X$ plot ($\sigma_k = 2.29 \times 10^9 \Omega/s^{0.21}$ for non-ideal Warburg behavior with the ideality factor equal to 0.21) has to be multiplied

by a correction factor of 1.12, and after that, the 'ideal' Warburg coefficient equals $\sigma = 2.57 \times 10^9 \Omega/s^{0.5}$. Here, we finally used the mean value of the determined Warburg constants (modified Bode plot, modified $R - X$ plot) to quantify the diffusion. The final obtained Warburg constant for MAPbI$_3$ perovskite single crystal with an ideality factor of 0.21 is thus equal to $\sigma = 2.53 \times 10^9 \Omega/s^{0.5}$. Once we are able to calculate the Warburg coefficient as described above, the diffusion coefficient can then be easily quantified according to the modified equation (2) as follows:

$$D = \left(\frac{RT}{\sigma c_{CV} n^2 F^2 A \sqrt{2}} \right)^2 = \left(\frac{RT}{\sigma_k \delta_{corr} c_{CV} n^2 F^2 A \sqrt{2}} \right)^2. \quad (8)$$

Note that other parameters from the equation, such as the dielectric constant of the material used and doping (defect) density calculated from Mott–Schottky analysis, were determined by impedance spectroscopy [28]. Final parameters obtained for all the measured crystals of different types (Cl$^-$, Br$^-$, I$^-$) are summarized in Table S1, Table S2, and Table S3 (see Supplementary Material). Consequently, we determined the diffusion coefficients for all three types of macroscopic single crystals: $D = (2.68 \pm 1.94) \times 10^{-8} \, \text{cm}^2/\text{s}$ for MAPbCl$_3$, $(1.12 \pm 0.61) \times 10^{-6} \, \text{cm}^2/\text{s}$ for MAPbBr$_3$ and $(3.63 \pm 2.36) \times 10^{-9} \, \text{cm}^2/\text{s}$ for MAPbI$_3$. Comparing these results with the ones published in the literature, we have to mention that the reported diffusion coefficient estimation differs vastly depending upon the measurement technique and sample preparation [54–60]. The overall diffusion coefficients for MAPbI$_3$ are comparable with the ones obtained by transient ion-drift measurements in thin films [55–57]. At the same time, both much higher and much lower values can be obtained depending on the method of measurements and sample preparation procedure. Transient absorption experiments using ultrafast microscopy [61] usually result in higher values for a diffusion coefficient, as it takes into account a contribution from both electrons and holes, while photoluminescence-based [27, 62–64] and electrical [28] measurements usually underestimate diffusion coefficient and diffusion length. Moreover, in the case of electrical measurements of lead halide perovskites, the presence of moisture and ambient conditions play a major role and, therefore, measurements obtained using non-encapsulated samples can differ radically.

4 Conclusion

In this study, we present a universal approach to quantify diffusion. The method is applied to lead halide perovskites, a material with mixed ionic–electronic conductivity that is widely used in electronics and optics. Although diffusion quantification using impedance spectroscopy has been previously described, there are several challenges that can arise in obtaining well-defined diffusion coefficients for the material, such as a material thickness larger than the diffusion length, non-idealities present in real-world systems, or a low-frequency range of the diffusion that makes it difficult to accurately locate the turnover frequency on the Nyquist plot. We describe how to overcome these challenges and accurately quantify the diffusion coefficient. It is worth noting that, while the described approach is specific to lead halide perovskites, it is also applicable to any other type of material.

5 Experimental

In this study, we applied our universal approach to three types of lead halide perovskite monocrystals: MAPbCl3, MAPbBr3, and MAPbI$_3$ synthesized by inverse temperature crystallization [32]. All three types of crystals, with various thicknesses, were analyzed to obtain reliable results and demonstrate the reproducibility of the method. The thickness of the crystals (the distance between the two electrodes) was in the range of millimeters, which was greater than the diffusion lengths in all cases. Additional information about the crystal synthesis and measurement equipment can be found in the supplementary information section.

Declarations

Conflict of interest The authors declare no conflicts of interest or personal relationships related to the work reported in this paper.

References

1. T.A. Kuku, A.M. Salau, Electrical conductivity of cusni3, cupbi3 and kpbi3. Solid State Ionics **25**(1), 1–7 (1987)
2. T. Kuku, Ionic transport and galvanic cell discharge characteristics of cupbi3 thin films. Thin Solid Films **325**(1–2), 246–250 (1998)
3. J. Wei, Y. Zhao, H. Li, G. Li, J. Pan, D. Xu, Q. Zhao, D. Yu, Hysteresis analysis based on the ferroelectric effect in hybrid perovskite solar cells. J. Phys. Chem. Lett. **5**(21), 3937–3945 (2014)
4. C.-S. Hsu, S.-C. Chang, D.E. Nikonov, I.A. Young, A. Naeemi, Hysteresis-free negative capacitance effect in metal-ferroelectric-insulator-metal capacitors with dielectric leakage and interfacial trapped charges. Phys. Rev. Appl. **15**(3), 034048 (2021)
5. M. Leoncini, R. Giannuzzi, A. Giuri, S. Colella, A. Listorti, V. Maiorano, A. Rizzo, G. Gigli, S. Gambino, Electronic transport, ionic activation energy and trapping phenomena in a polymer-hybrid halide perovskite composite. J. Sci. Adv. Mater. Dev. **6**(4), 543–550 (2021)
6. A. Gómez, Q. Wang, A.R. Goñi, M. Campoy-Quiles, A. Abate, Ferroelectricity-free lead halide perovskites. Energy Environ. Sci. **12**(8), 2537–2547 (2019)
7. A. Kovalenko, J. Pospisil, O. Zmeskal, J. Krajcovic, M. Weiter, Ionic origin of a negative capacitance in lead halide perovskites. Phys. Status Solidi (RRL) Rapid Res. Lett. **11**(3), 1600418 (2017)
8. D. Lan, The physics of ion migration in perovskite solar cells: Insights into hysteresis, device performance, and characterization. Prog. Photovolt. Res. Appl. **28**(6), 533–537 (2020)
9. B. Chen, M. Yang, S. Priya, K. Zhu, Origin of j-v hysteresis in perovskite solar cells. J. Phys. Chem. Lett. **7**(5), 905–917 (2016)
10. J.-P. Correa-Baena, S.-H. Turren-Cruz, W. Tress, A. Hagfeldt, C. Aranda, L. Shooshtari, J. Bisquert, A. Guerrero, Changes from bulk to surface recombination mechanisms between pristine and cycled perovskite solar cells. ACS Energy Lett. **2**(3), 681–688 (2017)
11. W. Tress, N. Marinova, T. Moehl, S. Zakeeruddin, M. Nazeeruddin, M. Grätzel, Energy Environ. Sci. **2015**(8), 995–1004 (2015)
12. S. van Reenen, M. Kemerink, H.J. Snaith, J. Phys. Chem. Lett. **6**, 3808–3814 (2015)
13. T.-Y. Yang, G. Gregori, N. Pellet, M. Grätzel, J. Maier, The significance of ion conduction in a hybrid organic-inorganic lead-iodide-based perovskite photosensitizer. Angew. Chem. Int. Ed. **54**(27), 7905–7910 (2015)
14. H. Yan, T. Ou, H. Jiao, T. Wang, Q. Wang, C. Liu, X. Liu, Y. Han, Y. Ma, C. Gao, Pressure dependence of mixed conduction and photo responsiveness in organolead tribromide perovskites. J. Phys. Chem. Lett. **8**(13), 2944–2950 (2017)
15. K. Yamada, Y. Kuranaga, K. Ueda, S. Goto, T. Okuda, Y. Furukawa, Phase transition and electric conductivity of asncl3 (a= cs and ch3nh3). Bull. Chem. Soc. Jpn. **71**(1), 127–134 (1998)
16. K. Yamada, T. Matsui, T. Tsuritani, T. Okuda, S. Ichiba, 127i-nqr, 119 sn mössbauer effect, and electrical conductivity of msni3 (m= k, nh4, rb, cs, and ch3nh3). Zeitschrift für Naturforschung A **45**(3–4), 307–312 (1990)
17. A. Dualeh, T. Moehl, N. Tétreault, J. Teuscher, P. Gao, M.K. Nazeeruddin, M. Gratzel, Impedance spectroscopic analysis of lead iodide perovskite-sensitized solid-state solar cells. ACS Nano **8**(1), 362–373 (2014)
18. J. Bisquert, A. Guerrero, C. Gonzales, Theory of hysteresis in halide perovskites by integration of the equivalent circuit. ACS Phys. Chem. Au **1**(1), 25–44 (2021)
19. M.A. Afroz, C.A. Aranda, N.K. Tailor, Yukta, P. Yadav, M.M. Tavakoli, M. Saliba, S. Satapathi, Impedance spectroscopy for metal halide perovskite single crystals: recent advances, challenges, and solutions. ACS Energy Lett. **6**(9), 3275–3286 (2021)
20. J. Jamnik, J. Maier, Treatment of the impedance of mixed conductors equivalent circuit model and explicit approximate solutions. J. Electrochem. Soc. **146**(11), 4183 (1999)
21. V. Butler, C. Catlow, B. Fender, J. Harding, Dopant ion radius and ionic conductivity in cerium dioxide. Solid State Ionics **8**(2), 109–113 (1983)
22. R.L. Cook, A.F. Sammells, On the systematic selection of perovskite solid electrolytes for intermediate temperature fuel cells. Solid State Ionics **45**(3–4), 311–321 (1991)
23. J. Carrillo, A. Guerrero, S. Rahimnejad, O. Almora, I. Zarazua, E. Mas-Marza, J. Bisquert, G. Garcia-Belmonte, Ionic reactivity at contacts and aging of methylammonium lead triiodide perovskite solar cells. Adv. Energy Mater. **6**(9), 1502246 (2016)
24. Z. Xiao, Y. Yuan, Y. Shao, Q. Wang, Q. Dong, C. Bi, P. Sharma, A. Gruverman, J. Huang, Giant switchable photovoltaic effect in organometal trihalide perovskite devices. Nat. Mater. **14**(2), 193–198 (2015)
25. A. Guerrero, J. You, C. Aranda, Y.S. Kang, G. Garcia-Belmonte, H. Zhou, J. Bisquert, Y. Yang, Interfacial degradation of planar lead halide perovskite solar cells. ACS Nano **10**(1), 218–224 (2016)
26. K. Domanski, J.-P. Correa-Baena, N. Mine, M.K. Nazeeruddin, A. Abate, M. Saliba, W. Tress, A. Hagfeldt, M. Gratzel, Not all that glitters is gold: metal-migration-induced degradation in perovskite solar cells. ACS Nano **10**(6), 6306–6314 (2016)
27. M. Lai, A. Obliger, D. Lu, C.S. Kley, C.G. Bischak, Q. Kong, T. Lei, L. Dou, N.S. Ginsberg, D.T. Limmer et al., Intrinsic anion diffusivity in lead halide perovskites is facilitated by a soft lattice. Proc. Natl. Acad. Sci. **115**(47), 11929–11934 (2018)
28. W. Peng, C. Aranda, O.M. Bakr, G. Garcia-Belmonte, J. Bisquert, A. Guerrero, Quantification of ionic diffusion in lead halide perovskite single crystals. ACS Energy Lett. **3**(7), 1477–1481 (2018)
29. G. Giorgi, K. Yamashita, M. Palummo, Nature of the electronic and optical excitations of ruddlesden-popper hybrid organic-inorganic perovskites: The role of the many-body interactions. J. Phys. Chem. Lett. **9**(19), 5891–5896 (2018)
30. L. Mao, C.C. Stoumpos, M.G. Kanatzidis, Two-dimensional hybrid halide perovskites: principles and promises. J. Am. Chem. Soc. **141**(3), 1171–1190 (2018)
31. C.M. Mauck, W.A. Tisdale, Excitons in 2d organic-inorganic halide perovskites. Trends Chem. **1**(4), 380–393 (2019)
32. M.I. Saidaminov, A.L. Abdelhady, B. Murali, E. Alarousu, V.M. Burlakov, W. Peng, I. Dursun, L. Wang, Y. He, G. Maculan et al., High-quality bulk hybrid perovskite single crystals within minutes by inverse temperature crystallization. Nat. Commun. **6**(1), 1–6 (2015)
33. S.-S. Rong, M.B. Faheem, Y.-B. Li, Perovskite single crystals: Synthesis, properties, and applications. J. Electron. Sci. Technol. **19**(2), 100081 (2021)
34. V. Vivier, M.E. Orazem, Impedance analysis of electrochemical systems. Chem. Rev. **122**(12), 11131–11168 (2022)
35. A. Guerrero, J. Bisquert, G. Garcia-Belmonte, Impedance spectroscopy of metal halide perovskite solar cells from the perspective of equivalent circuits. Chem. Rev. **121**(23), 14430–14484 (2021)
36. X. Gong, Z. Huang, R. Sabatini, C.-S. Tan, G. Bappi, G. Walters, A. Proppe, M.I. Saidaminov, O. Voznyy, S.O. Kelley et al., Contactless measurements of photocarrier transport properties in perovskite single crystals. Nat. Commun. **10**(1), 1–7 (2019)
37. O.V. Mikhnenko, P.W. Blom, T.-Q. Nguyen, Exciton diffusion in organic semiconductors. Energy Environ. Sci. **8**(7), 1867–1888 (2015)
38. S. Taylor, E. Gileadi, Physical interpretation of the warburg impedance. Corrosion **51**(09), (1995)

39. E. Warburg, Ueber das verhalten sogenannter unpolarisirbarer elektroden gegen wechselstrom. Ann. Phys. **303**(3), 493–499 (1899)

40. J. Bisquert, Theory of the impedance of electron diffusion and recombination in a thin layer. J. Phys. Chem. B **106**(2), 325–333 (2002)

41. M. Janssen, J. Bisquert, Locating the frequency of turnover in thin-film diffusion impedance. J. Phys. Chem. C **125**(28), 15737–15741 (2021)

42. Z. Lukács, T. Kristóf, A generalized model of the equivalent circuits in the electrochemical impedance spectroscopy. Electrochim. Acta **363**, 137199 (2020)

43. V. Freger, Diffusion impedance and equivalent circuit of a multilayer film. Electrochem. Commun. **7**(9), 957–961 (2005)

44. V. Feliu, J. González, C. Andrade, S. Feliu, Equivalent circuit for modelling the steel-concrete interface. i. experimental evidence and theoretical predictions. Corros. Sci. **40**(6), 975–993 (1998)

45. N. Sekushin, Equivalent circuit of warburg impedance. Russ. J. Electrochem. **45**(7), 828–832 (2009)

46. V. Muralidharan, Warburg impedance-basics revisited. Anti-Corrosion Methods and Materials (1997)

47. F. Ebadi, M. Aryanpour, R. Mohammadpour, N. Taghavinia, Coupled ionic-electronic equivalent circuit to describe asymmetric rise and decay of photovoltage profile in perovskite solar cells. Sci. Rep. **9**(1), 1–9 (2019)

48. S.-M. Yoo, S.J. Yoon, J.A. Anta, H.J. Lee, P.P. Boix, I. Mora-Sero, An equivalent circuit for perovskite solar cell bridging sensitized to thin film architectures. Joule **3**(10), 2535–2549 (2019)

49. E. Von Hauff, Impedance spectroscopy for emerging photovoltaics. J. Phys. Chem. C **123**(18), 11329–11346 (2019)

50. Z. Zhang, D. Chen, C. Chang, Improved electrochemical performance of lini 0.8 co 0.1 mn 0.1 o 2 cathode materials via incorporation of rubidium cations into the original li sites. RSC Adv. **7**(81), 51721–51728 (2017)

51. P. Xiao, Y. Cai, X. Chen, Z. Sheng, C. Chang, Improved electrochemical performance of life 0.4 mn 0.6 po 4/c with cr 3+ doping. RSC Adv. **7**(50), 31558–31566 (2017)

52. B. Csomós, D. Fodor, I. Vajda, Estimation of battery separator area, cell thickness and diffusion coefficient based on non-ideal liquid-phase diffusion modeling. Energies **13**(23), 6238 (2020)

53. M. Oldenburger, B. Beduerftig, A. Gruhle, F. Grimsmann, E. Richter, R. Findeisen, A. Hintennach, Investigation of the low frequency warburg impedance of li-ion cells by frequency domain measurements. J. Energy Storage **21**, 272–280 (2019)

54. M.H. Futscher, M.K. Gangishetty, D.N. Congreve, B. Ehrler, Quantifying mobile ions and electronic defects in perovskite-based devices with temperature-dependent capacitance measurements: Frequency vs time domain. J. Chem. Phys. **152**(4), 044202 (2020)

55. M.H. Futscher, J.M. Lee, L. McGovern, L.A. Muscarella, T. Wang, M.I. Haider, A. Fakharuddin, L. Schmidt-Mende, B. Ehrler, Quantification of ion migration in ch 3 nh 3 pbi 3 perovskite solar cells by transient capacitance measurements. Mater. Horiz. **6**(7), 1497–1503 (2019)

56. L. McGovern, I. Koschany, G. Grimaldi, L.A. Muscarella, B. Ehrler, Grain size influences activation energy and migration pathways in mapbbr3 perovskite solar cells. J. Phys. Chem. Lett. **12**(9), 2423–2428 (2021)

57. D.R. Ceratti, A. Zohar, R. Kozlov, H. Dong, G. Uraltsev, O. Girshevitz, I. Pinkas, L. Avram, G. Hodes, D. Cahen, Eppur si muove: proton diffusion in halide perovskite single crystals. Adv. Mater. **32**(46), 2002467 (2020)

58. M. Karlsson, Z. Yi, S. Reichert, X. Luo, W. Lin, Z. Zhang, C. Bao, R. Zhang, S. Bai, G. Zheng et al., Mixed halide perovskites for spectrally stable and high-efficiency blue light-emitting diodes. Nat. Commun. **12**(1), 1–10 (2021)

59. M. Sajedi Alvar, P.W. Blom, G.-J.A. Wetzelaer, Space-charge-limited electron and hole currents in hybrid organic-inorganic perovskites. Nat. Commun. **11**(1), 1–9 (2020)

60. M. García-Batlle, J. Mayen Guillen, M. Chapran, O. Baussens, J. Zaccaro, J.-M. Verilhac, E. Gros-Daillon, A. Guerrero, O. Almora, G. Garcia-Belmonte, Coupling between ion drift and kinetics of electronic current transients in mapbbr3 single crystals. ACS Energy Lett. **7**(3), 946–951 (2022)

61. Z. Guo, J.S. Manser, Y. Wan, P.V. Kamat, L. Huang, Spatial and temporal imaging of long-range charge transport in perovskite thin films by ultrafast microscopy. Nat. Commun. **6**(1), 1–8 (2015)

62. G. Xing, N. Mathews, S.S. Lim, N. Yantara, X. Liu, D. Sabba, M. Grätzel, S. Mhaisalkar, T.C. Sum, Low-temperature solution-processed wavelength-tunable perovskites for lasing. Nat. Mater. **13**(5), 476–480 (2014)

63. T.J. Savenije, C.S. Ponseca Jr., L. Kunneman, M. Abdellah, K. Zheng, Y. Tian, Q. Zhu, S.E. Canton, I.G. Scheblykin, T. Pullerits et al., Thermally activated exciton dissociation and recombination control the carrier dynamics in organometal halide perovskite. J. Phys. Chem. Lett. **5**(13), 2189–2194 (2014)

64. S.D. Stranks, V.M. Burlakov, T. Leijtens, J.M. Ball, A. Goriely, H.J. Snaith, Recombination kinetics in organic-inorganic perovskites: excitons, free charge, and subgap states. Phys. Rev. Appl. **2**(3), 034007 (2014)